



www.eurjic.org

Enhanced Anodic 5-Hydroxymethylfurfural Oxidation toward Efficient Overall CO₂ Electrolysis

Fangyun Su, Zixian Ye, Zhenhai Zhao, Hongyu Jiao, Kefeng Wu, Jiawang Di, Yu Li,* and Tongbu Lu*

Electrocatalytic reduction of CO₂ into value-added chemicals provides an appealing approach to mitigating the carbon-emission issues. However, the kinetically sluggish anodic oxygen evolution reaction (OER) not only consumes a large part of the electricity but also produces O₂ of low value, thus severely limiting the economy of overall CO₂ electrolysis. Herein, a biomass upgradecoupled CO₂ reduction reaction (CO₂RR) strategy is developed that 5-hydroxymethylfurfural oxidation reaction (HMFOR) is substituted for the traditional OER to selective produce high value-added 2,5-furanodiformic acid (FDCA) rather than O2 in the anode side of the overall CO2 electrolysis. A Ni foamsupported sea urchin-like NiCo₂O₄ anode (NiCo₂O₄@NF) is successfully fabricated with a high Faradaic efficiency of 96.7% for FDCA in HMFOR. In-situ electrochemical impedance spectroscopic and Raman spectroscopic measurements revealed that the Ni²⁺ ↔ Ni³⁺ transformation with favored adsorption of OH⁻ promotes HMFOR. Moreover, a two-electrode cell featuring anodic HMFOR and cathodic CO₂RR was assembled to simultaneously produce FDCA and formic acid. Compared with the traditional CO₂RR-OER couple, the energy requirement is significantly reduced by 22.9% by the CO₂RR-HMFOR couple. Furthermore, an efficient solar-driven electrocatalytic CO2RR-HMFOR system is established with excellent performance, demonstrating the viability of the coupling strategy.

reduce the dependence on fossil resources.[14,15] In particular,

1. Introduction

Electrochemical CO₂ reduction to value-added chemicals is a two-birds with one-stone strategy that concurrently transforms the unstable renewable electricity into stable chemical energy and alleviates the climate issue due to the excessive carbon emission.^[1–5] However, the energy efficiency of traditional overall CO₂ electrolysis is severely restricted by the kinetically sluggish anodic OER which involves four-electron transfer and requires large overpotentials. [6,7] Moreover, the anodic OER mainly produces O₂ of low value that drastically limits the production value per kW h of electricity, and the byproduct reactive oxygen species such as H₂O₂ can decompose the ion exchange membrane, leading to undesired damage of the electrolyzer. Therefore, substituting the OER with other high value-added anodic oxidation reactions with lower energy requirements may shed light on the aforementioned problems of overall CO₂ electrolysis.^[8–13]

As an extensive and renewable resource, biomass can be converted into highly value-added fine chemicals as well as fuels to

F. Su. Z. Zhao, H. Jiao, K. Wu Petrochina Lanzhou Petrochemical Company Lanzhou, Gansu 730060, China

Z. Ye, J. Di, Y. Li, T. Lu

Institute for New Energy Materials and Low Carbon Technologies School of Materials Science and Engineering

Tianjin University of Technology

Tianjin 300384, China E-mail: yli@email.tjut.edu.cn

doi.org/10.1002/ejic.202500133

lutongbu@tjut.edu.cn Supporting information for this article is available on the WWW under https://

MOE International Joint Laboratory of Materials Microstructure

5-hydroxymethylfurfural (HMF), a typical biomass-based platform compound derived from the abundant plant cellulose, is a promising candidate for the anodic reactant of overall CO₂ electrolysis.[16-21] Benefitting from the more favorable thermodynamics of 5-hydroxymethylfurfural oxidation reaction and (HMFOR), its standard potential (0.30 V) is much lower than that of OER (1.23 V).[17,22,23] In addition, HMF can be converted into 2,5-furandicarboxylic acid (FDCA), a valuable monomer for the production of bio-renewable polymers such as polyethylene furandicarboxylate, thus reducing the fossil fuel consumption and environmental pollution. [24-27] Compared to other anodic oxidation reactions such as NaCl-to-Cl₂, glycerol-to-lactic acid, furfural-to-2-furoic acid, and glucose-to-gluconic acid, HMF-to-FDCA shows the highest added value considering the market price differences of raw material and corresponding product.[12] However, selective production of FDCA from HMF requires the complete oxidation of the formyl and the alcohol groups in HMF molecule without further C—C bond cleavage, which is guite challenging. [28,29] For instance, a mixture of maleic acid and formic acid was obtained when PdO was employed as the catalyst for HMFOR, suggesting the C—C bond cleavage during oxidation. [29] Therefore, it is highly demanded to develop efficient anodes that can selectively convert HMF into FDCA.

For the cathodic CO₂ reduction reaction (CO₂RR), albeit various C_1 (e.g., CO, HCOOH, and CH₄) and C_2 (e.g., C_2H_4 and C_2H_5OH) products have been successfully obtained, [30] techno-economic analysis revealed that HCOOH holds the highest viability. [31,32] Given this, we are motivated to develop an efficient paired electrolysis system comprising anodic HMFOR-to-FDCA and cathodic CO₂RR-to-HCOOH. The half-cell and overall reactions involving in the coupling system are shown below.

(1)

(2)

Cathode reaction: $3CO_2 + 6e^- + 6H^+ \rightarrow 3HCOOH$

Overall reaction: $3CO_2 + HMF + 2H_2O \rightarrow 3HCOOH + FDCA$ (3)

Herein, an efficient electrode featuring Ni foam-supported sea urchin-like spinel catalyst (NiCo₂O₄@NF) was fabricated for selective production of FDCA in the anodic HMFOR. Compared to OER, the potential was sharply reduced by 160 mV at a current density of 50 mA cm⁻², with the Faradaic efficiency (FE) and yield of FDCA both close to 100%. In-situ electrochemical impedance spectroscopy and in-situ Raman spectroscopy were conducted to uncover the reaction mechanism and dynamical structure evolution of NiCo₂O₄@NF. The results showed that the evolution of Ni sites under positive potential enhanced the adsorption of OH-, and the formed NiOOH species facilitated the oxidation of HMF and intermediates to FDCA. For the cathodic CO₂RR, Cu foamsupported Bi nanosheets electrode (Bi NSs@CF) with high surface area was prepared via a facile galvanic replacement process followed by an electrochemical reconstruction strategy. As a result, HMFOR and CO₂RR were successfully coupled in a two-electrode overall cell with high FEs and significant improved energy efficiencies. As a step further, the CO₂RR-HMFOR couple was adapted into a photovoltaic electrolyzing system, which exhibited impressive conversion efficiencies up to 1.2% and 0.7% for solar-to-FDCA and solar-to-HCOOH under illumination, respectively. This work shows the importance of the coupling strategy in improving the economic feasibility of CO₂RR technique.

2. Results and Discussion

The NiCo₂O₄@NF was synthesized via a hydrothermal method followed by calcination. For comparison, Ni foam-supported Co₃O₄ (denoted as Co₃O₄@NF) was also prepared in the similar way except for the absence of Ni precursor. The detailed information was described in the Supporting Information. Xray diffraction (XRD) patterns for these two catalysts both exhibit characteristic peaks at 31.1°, 36.7°, 44.6°, 59.1°, and 64.9°, which can be assigned to the (220), (311), (400), (511), (440) planes of NiCo₂O₄ (PDF#20-0781)/Co₃O₄ (PDF#42-1467), respectively, revealing their spinel structure (Figure S1, Supporting Information). Scanning electron microscopy (SEM) characterization was performed to look into the morphology of the two electrodes. As shown in Figure 1a, numerous nanoneedles were observed over the Ni foam support and assembled in sea urchin shape for NiCo₂O₄@NF. The diameter and length of the nanoneedles are about 50 and 960 nm, respectively. In comparison, nanosheet- and nanoneedle-like structure Co₃O₄ were distributed over Ni foam support for Co₃O₄@NF (Figure S2, Supporting Information). To get insight into the surface crystalline structure of NiCo₂O₄@NF, high-resolution transmission electron microscopy (HRTEM) were conducted. Figure 1b displays clear lattice fringes with interplanar spacings of 0.24 and 0.28 nm, corresponding to the (311) and (220) planes of NiCo₂O₄, respectively. The multiple diffraction spots observed in the selected area electron diffraction (SAED) pattern (inset of Figure 1b) demonstrate the polycrystalline feature of NiCo₂O₄@NF, indicative of the abundant exposed facets.

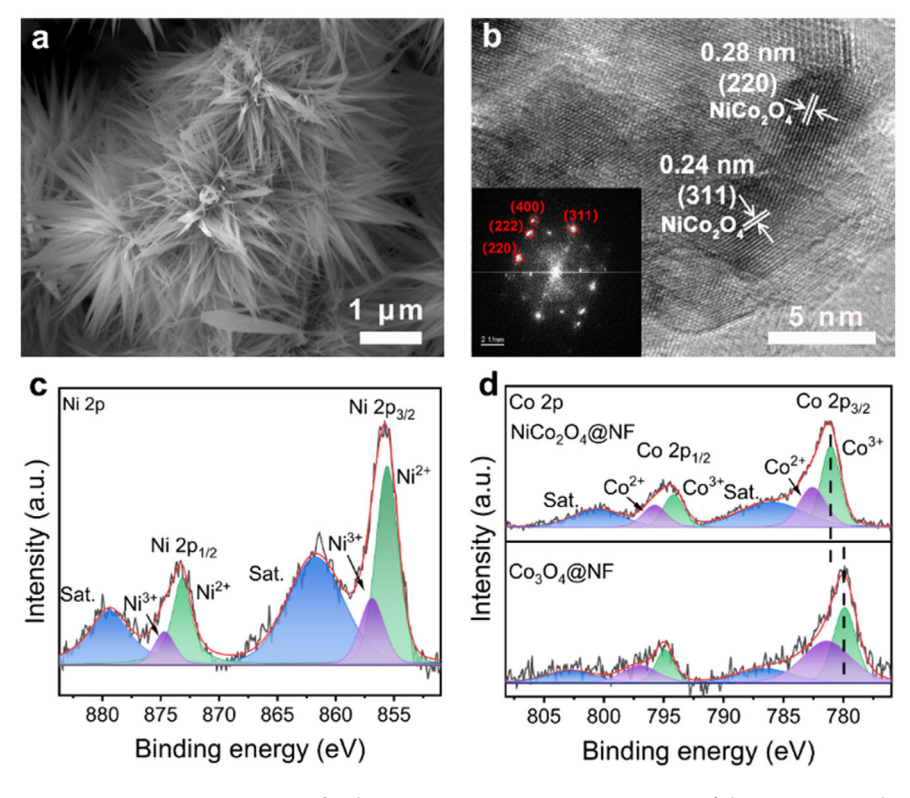


Figure 1. a) SEM and b) HRTEM images (inset: SAED pattern) for the NiCo₂O₄@NF. c) Ni 2p XPS spectrum of the NiCo₂O₄@NF. d) Co 2p XPS spectra of the NiCo₂O₄@NF and Co₃O₄@NF.

The chemical states of Ni and Co in NiCo2O4@NF were ascertained by X-ray photoelectron spectroscopy (XPS). The highresolution XPS spectrum of the Ni 2p was depicted in Figure 1c. A strong peak located at 855.9 eV that ascribes to the Ni^{2+} $2p_{3/2}$ is observed, whereas only a weak peak belonging to Ni^{2+} $2p_{3/2}$ exists, suggesting that the introduced Ni atoms mainly occupy the Co²⁺ sites at the tetrahedral voids in the spinel Co₃O₄.^[33] This was also verified by Co 2p XPS spectra of NiCo₂O₄@NF and Co₃O₄@NF (Figure 1d). The deconvoluted Co 2p spectrum for Co₃O₄@NF displays distinct peaks at 779.9 and 781.6 eV, which can be assigned to the $Co^{3+} 2p_{3/2}$ and $Co^{2+} 2p_{3/2}$ signals, respectively. In sharp contrast, the peak intensity corresponding to Co²⁺ 2p_{3/2} significantly decreases for NiCo₂O₄@NF, signifying the reduced proportion of Co²⁺ owing to the Ni²⁺ substitution.^[34–36] In addition, the binding energy of Co³⁺ 2p_{3/2} in NiCo₂O₄@NF positively shifts to 781.1 eV, suggesting the decreased electron density of Co sites due to the electron interaction between Co and Ni atoms.[37] Besides, a near 1:2 atomic ratio between Ni and Co was obtained according to the XPS survey spectrum of NiCo₂O₄@NF, which also indicates the successful substitution of Co²⁺ by Ni²⁺ (Figure S3, Supporting Information).

The HMFOR performance was assessed in a solution containing 1.0 M KOH + 10 mM HMF using a three-electrode system. As revealed by the linear sweep voltammetry (LSV) curves in Figure 2a, it only requires 1.36 V versus reversible hydrogen electrode (vs RHE) for NiCo₂O₄@NF to achieve a current density of 50 mA cm⁻², 160 mV lower than that of OER at identical current density, indicating the more favorable kinetics for HMFOR. Moreover, in comparison with Co₃O₄@NF, NiCo₂O₄@NF displayed markedly reduced overpotentials in both OER and HMFOR, signifying that the introduction of Ni sites effectively facilitate the reactions. This is also verified by the Tafel analysis, as shown in Figure S4, Supporting Information. The NiCo₂O₄@NF displays a Tafel slope of 178.5 mV dec⁻¹, much smaller than that for Co₃O₄@NF (319.1 mV dec⁻¹). The lower Tafel slope contributes to a faster increment of HMF conversion rate with increasing overpotential, demonstrating the superior activity of NiCo₂O₄@NF in HMFOR. To gain insight into the intrinsic activities of

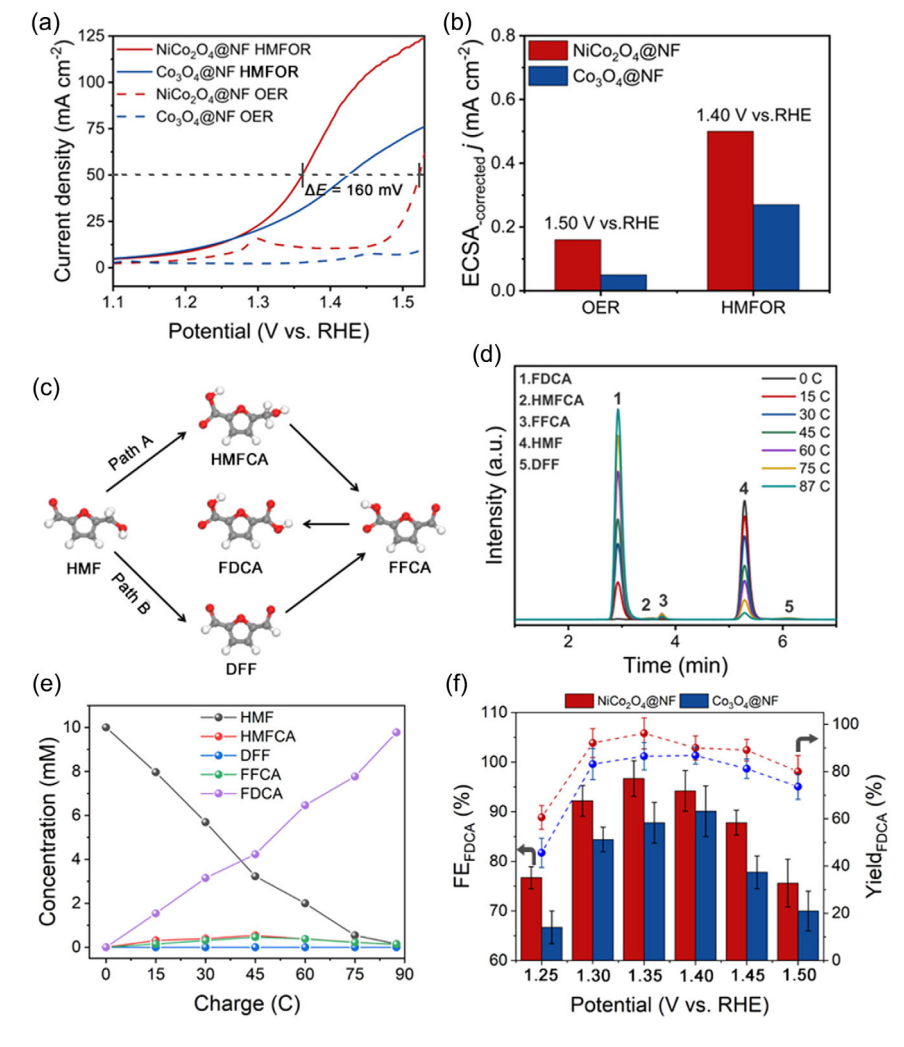


Figure 2. a) Linear sweep voltammetry (LSV) curves and b) ECSA_{corrected} j of NiCo₂O₄@NF and Co₃O₄@NF in OER and HMFOR, c) The possible pathways of HMF oxidation to FDCA. d) HPLC chromatograms and e) corresponding concentration changes of HMF possible oxidation products as charge accrues at 1.35 V by NiCo₂O₄@NF. f) Faradaic efficiencies and yields of FDCA at different potentials for NiCo₂O₄@NF and Co₃O₄@NF in HMFOR; the data was obtained with at least three replicates.

NiCo₂O₄@NF and Co₃O₄@NF, their electrochemical surface area (ECSA) was obtained by estimating their electrochemical double-layer capacitance (C_{cll}) in the non-Faradaic regions using cyclic voltammetry (CV) scans (Figure S5, Supporting Information). The C_{dl} values of NiCo₂O₄@NF and Co₃O₄@NF are calculated to be 156.6 and 153.5 mF cm⁻², respectively, suggesting that the introduction of Ni into Co₃O₄ hardly changes the active surface area. ECSA-corrected current densities were presented to clearly show the intrinsic activities of different catalysts (Figure 2b). NiCo₂O₄@NF exhibits ECSA-corrected j of 0.16 mA cm⁻² in OER and 0.50 mA cm⁻² in HMFOR, which are 3.20 and 1.85 times as high as that by Co₃O₄@NF in OER and HMFOR, respectively. For both HMFOR and OER in alkaline electrolyte, the adsorption and activation of OH⁻ plays a pivotal role.[38,39] Accordingly, we investigated the adsorption strength of OH⁻ on NiCo₂O₄@NF and Co₃O₄@NF through the OH⁻ adsorption test. As depicted by the oxidative LSV curves in Ar-saturated 1.0 M KOH aqueous solution, the potential of OH⁻ adsorption for NiCo₂O₄@NF is 20 mV lower than that for Co₃O₄@NF, evidencing that the Ni sites promote the adsorption of OH⁻ for the improved performance.[40]

The oxidation of HMF to FDCA can proceed via two paths: One begins with the oxidation of aldehyde to form 5-hydroxymethyl-2-furancarboxylic acid (HMFCA); the other path takes place through the alcohol oxidation to form 2,5-diformylfuran (DFF). [16] Then the HMFCA/DFF is further oxidized into 2-formyl-5-furancarboxylic acid (FFCA) and finally FDCA (Figure 2c). Therefore, HPLC was employed to detect the possible reaction intermediates. As displayed by the HPLC chromatograms

recorded at 1.35 V versus RHE in Figure 2d, with the charge increasing, the peak belonging to FDCA grows stronger, whereas the intensity of peak assigned to HMF decreases. The corresponding concentrations of the all five chemicals were calculated according the calibration curves (Figure 2e; Figure S7, Supporting Information). Notably, the concentration of HMFCA gradually increased as the charge increased, and the maximum concentration emerged at the charge of 45 C followed by decrease in concentration (Figure S8, Supporting Information). Similar trend was also observed for FFCA. On the contrary, barely no DFF was detected throughout the process. These results prove that the HMFOR begins with the oxidation of the aldehyde group rather than the alcohol group. The FEs and yields of FDCA under different potentials were presented in Figure 2f. The total charge was kept at 87.6 C according to the theoretical consumption of electrons for complete conversion of the added HMF. Impressively, NiCo₂O₄@NF exhibits significantly higher FE_{FDCA} than that by Co₃O₄@NF within the tested potential window. The highest FE and yield of FDCA reached 96.7% and 96.2% at 1.35 V versus RHE by NiCo₂O₄@NF, respectively, whereas the optimal values achieved by Co₃O₄@NF were only 90.1% and 86.8% at 1.40 V versus RHE, respectively. Besides, higher FEFDCA and YieldFDCA were achieved by NiCo₂O₄@NF within the potential window, signifying its superior HMFOR performance. To evaluate the HMFOR stability of NiCo₂O₄@NF, a cyclic test comprising eight consecutive cycles was carried out (Figure S9, Supporting Information). As a result, the FEs and yields of FDCA were maintained above 90% during the whole electrolysis, demonstrating the excellent stability of NiCo₂O₄@NF in HMFOR.

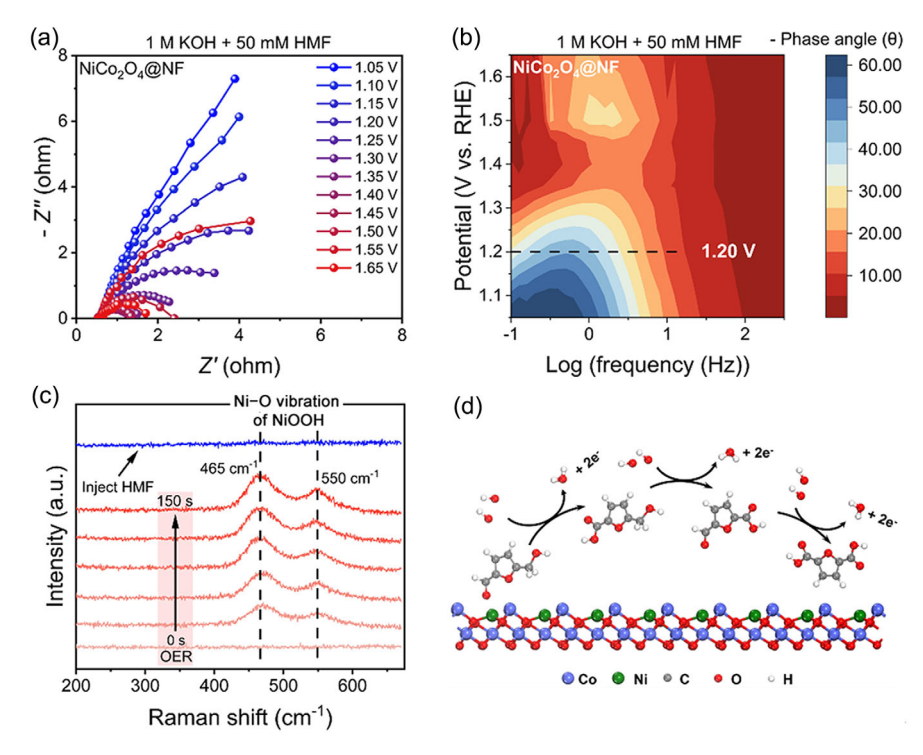


Figure 3. In-situ potential-dependent a) Nyquist plots and b) corresponding contour-type Bode plots of NiCo₂O₄@NF in 1.0 M KOH with 50 mM HMF. c) In-situ time-dependent Raman spectra of NiCo₂O₄@NF during OER (1.0 M KOH) and after injection of 50 mM HMF under 1.35 V vs. RHE. d) Proposed reaction mechanism of HMF oxidation over NiCo₂O₄@NF.

In-situ potential-dependent EIS measurements were first conducted to gain in-depth understanding on the enhanced performance of NiCo₂O₄@NF. As revealed by the Nyquist plots of NiCo₂O₄@NF in Figure 3a, approximately vertical lines were observed within the low potentials ranging 1.05-1.15 V versus RHE. A semicircle emerged as the potential increased to 1.20 V versus RHE, suggesting the beginning of the Faradaic reaction.[41] In comparison, a higher potential of 1.30 V versus RHE was required by Co₃O₄@NF to start HMFOR (Figure S10, Supporting Information). Moreover, smaller radius of semicircles was observed for NiCo₂O₄@NF compared with that for Co₃O₄@NF under identical potential, indicating the improved charge transfer between catalyst and substrate. The corresponding in-situ contour-type Bode plots were shown in Figure 3b. The peak at low frequency (10⁻¹–10¹ Hz) can be ascribed to nonhomogeneous charge distribution owing to the formation of oxidized species on the electrode surface. [42] An apparent transition peak emerged at the potential of 1.20 versus RHE for NiCo₂O₄@NF, which was 60 mV lower than that for $Co_3O_4@NF$, suggesting the promoted HMF oxidation with the existence of Ni sites (Figure S11, Supporting Information).^[41]

As indicated in Figure 2a, an obvious peak arises at $1.29\,\mathrm{V}$ versus RHE for $\mathrm{NiCo_2O_4@NF}$ in OER, which can be assigned to the oxidation of $\mathrm{Ni^{2+}}$ to $\mathrm{Ni^{3+}}$. In contrast, only a weak peak at $1.45\,\mathrm{V}$ versus RHE was observed for $\mathrm{Co_3O_4@NF}$ in OER. Therefore, we inferred that the promoted activation of $\mathrm{OH^-}$ through the thermodynamically more favourable transformation of $\mathrm{Ni^{2+}}$ to $\mathrm{Ni^{3+}}$ contributed to the enhanced HMFOR on $\mathrm{NiCo_2O_4@NF}$. To verify this deduction, valence state analysis of Ni and Co in $\mathrm{NiCo_2O_4@NF}$ before and after electrooxidation of HMF at $1.35\,\mathrm{V}$ versus RHE was carried out (Figure S12, Supporting Information). Compared to the fresh $\mathrm{NiCo_2O_4@NF}$, the ratio of $\mathrm{Ni^{3+}}$ to $\mathrm{Ni^{2+}}$ in the Ni 2p XPS spectrum fitted after HMFOR increased from 0.56 to 0.79, signifying the conversion of $\mathrm{Ni^{2+}}$ to $\mathrm{Ni^{3+}}$ during HMFOR (Table S1, Supporting Information). On the contrary, the $\mathrm{Co^{3+}/Co^{2+}}$ ratio before and after HMFOR were

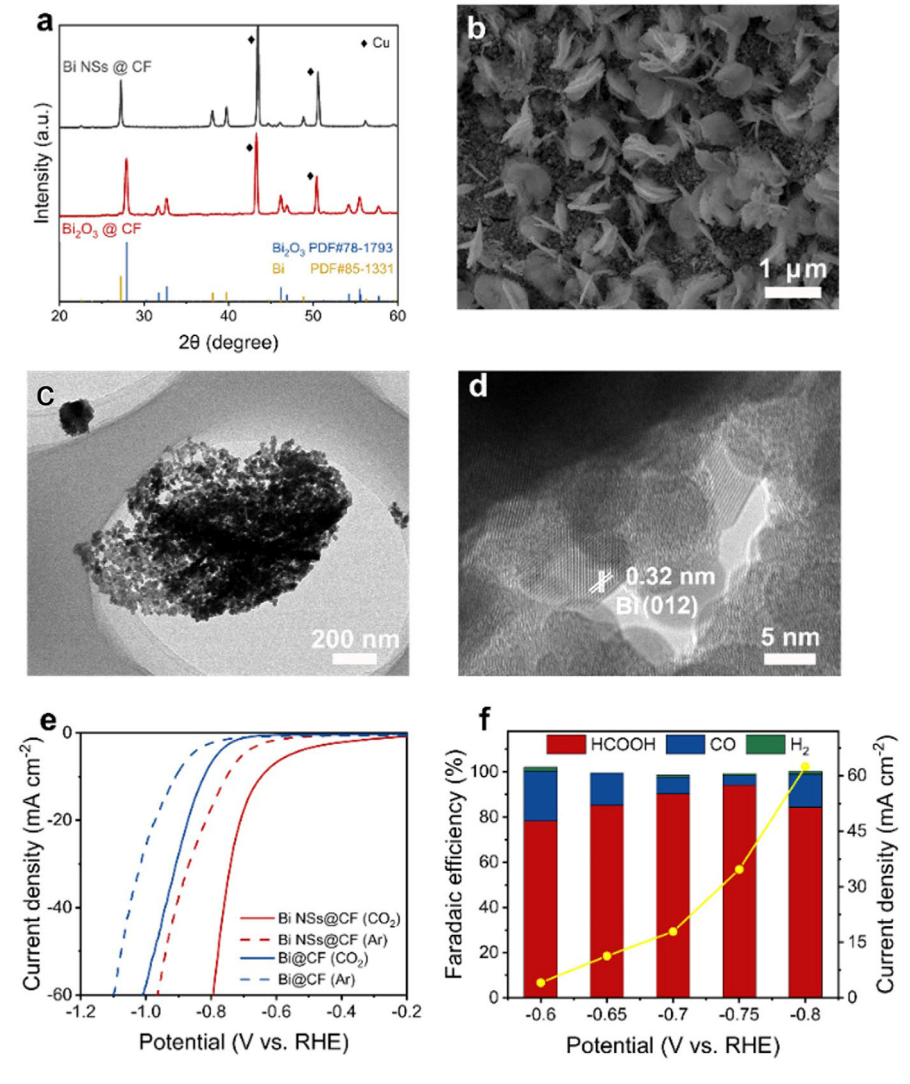


Figure 4. Characterization and CO₂RR performance of Bi NSs@CF. a) XRD patterns of Bi₂O₃@CF and Bi NSs@CF. b) SEM, c) TEM, and d) HRTEM images of Bi NSs@CF. e) LSV curves of Bi NSs@CF (red line) and Bi@CF (blue line) in Ar- or CO₂-saturated 1.0 M KHCO₃ solutions. f) Faradaic efficiencies of CO₂RR products and current densities for Bi NSs@CF at different potentials.

Chemistry Europe

European Chemical Societies Publishing

0.69 and 0.70, respectively, demonstrating that the Ni³⁺ sites are the active species in HMFOR.^[43] To further disclose the formation of Ni³⁺ species, in-situ time-dependent Raman spectra were recorded (Figure 3c; Figure S13, Supporting Information). With a potential of 1.35 V versus RHE applied, two characteristic peaks located at 465-550 cm⁻¹ assigned to the Ni-O vibrations of NiOOH species appeared, and grew stronger as the reaction time increased. [41] Notably, these two peaks disappeared immediately after the injection of HMF, suggesting that the NiOOH was consumed during HMFOR. On the basis of the above results, it can be safely deduced that during HMFOR, the Ni²⁺ is electrooxidized into Ni³⁺ with the formation of NiOOH. Subsequently, the electrophilic *OH in NiOOH attacks the nucleophilic aldehyde and alcohol groups of HMF through a series of dehydration process, and finally generates FDCA. The proposed reaction pathway was illustrated in Figure 3d.

Cu foam-supported Bi nanosheets electrode (Bi NSs@CF) was fabricated through an electrochemical reconstruction strategy for cathodic CO₂RR, and the detailed information was described in the Supporting Information. Firstly, Bi particles were grown on the CF surface via a galvanic replacement process, and the as-prepared catalyst was denoted as Bi@CF (Figure S14, Supporting Information). After calcined in air atmosphere, CF-supported Bi₂O₃ was obtained (denoted as Bi₂O₃@CF; Figure S15, Supporting Information). Subsequently, the Bi₂O₃@CF was employed as the working electrode and treated under a series of negative potentials in CO₂-saturated KHCO₃ solution. The Bi₂O₃ was successfully reduced to Bi after the electrochemical treatment according to the XRD results (Figure 4a). Interestingly,

SEM and TEM images show that sheet-like structures with rich pores were formed over the CF support after the electrochemical treatment (Figure 4b.c). Clear lattice fringes with interplanar space of 0.32 nm that correspond to Bi(012) plane were observed in the HRTEM image for Bi NSs@CF (Figure 4d). The porous nanosheets are composed of Bi grains with an average size of 5 nm. The CO₂RR performance of Bi NSs@CF was assessed in an H-type cell using three-electrode system. As revealed by the cathodic LSV curves in Figure 4e, both Bi NSs@CF and Bi@CF exhibited improved current densities when CO₂ was introduced into the electrolyte, demonstrating the favoured CO₂RR for bismuth. Impressively, marked higher current densities were achieved by Bi NSs@CF than that by Bi@CF at identical potentials, which can be attributed to the abundant active Bi sites and promoted charge transfer benefitting from the porous nanosheet structure. This was also verified by the ECSA and EIS results. Bi NS@CF displays a $C_{\rm dl}$ up to 50.2 mF cm⁻², which is 2.22 times as high as that for Bi@CF (Figure S16, Supporting Information). The EIS spectrum of Bi NS@CF exhibits a smaller semicircle than that by Bi@CF, indicative of its faster interfacial charge transfer during CO₂RR (Figure \$17, Supporting Information), Figure 4f shows the FEs of different products and corresponding current densities under various potentials for Bi NSs@CF. At a potential of -0.75 V versus RHE, a maximum FE of 94.7% for HCOOH is achieved. Moreover, the FEs for HCOOH remain over 80% within the potential window, suggesting the compatibility to anodic HMFOR.

Inspired by the above results, a two-electrode electrolyzer comprising cathodic CO₂RR and anodic HMFOR was assembled using Bi NSs@CF and NiCo₂O₄@NF, respectively. As a result,

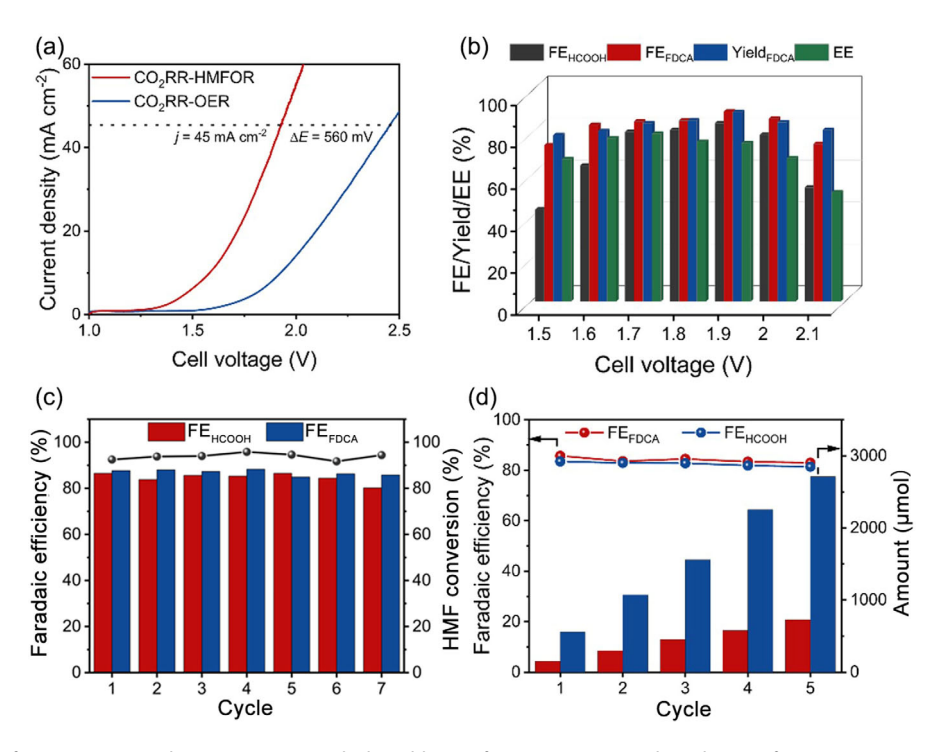


Figure 5. a) LSV curves for CO_2RR -OER and CO_2RR -HMFOR (with the addition of 10 mm HMF in anolyte). b) FEs of HCOOH/FDCA, yields of FDCA and total energy efficiencies (EEs) of CO_2RR -HMFOR at different potentials. c) Cyclic test of CO_2RR -HMFOR. The analyte was refreshed for each cycle. d) Performance of solar-driven CO_2RR -HMFOR using a photovoltaic system. Extra HMF was added into the anolyte at the beginning of each cycle to keep the concentration of HMF at 10 mm.



coupling cathodic CO₂RR with energy-efficient anodic HMFOR (CO₂RR-HMFOR) prominently reduced the full cell voltage (Figure 5a). A cell voltage of only 1.58 V was required to deliver a current density of 10 mA cm⁻² for CO₂RR-HMFOR. In sharp contrast, the cell voltage increased to 1.89 V to achieve identical current density when coupling CO₂RR with conventional OER (CO₂RR-OER). Moreover, at a higher current density of 45 mA cm⁻², the cell voltage for CO₂RR-HMFOR was 560 mV lower than that of CO₂RR-OER, which indicates a 22.9% reduction in electricity consumption. The yields of FDCA, FEs of HCOOH/ FDCA, and the total energy efficiencies (EEs) under various cell voltages (from 1.5 to 2.1 V) of CO₂RR-HMFOR were displayed in Figure 5b. As anticipated, the CO₂RR-HMFOR couple shows outstanding FEs for HCOOH and FDCA with over 80% yields of FDCA. Over voltages ranging from 1.7 to 2.0 V, the FEs of FDCA and HCOOH surpass 80% and 85%, respectively, with over 60% EEs. Notably, the FEs of FDCA and HCOOH concurrently reach the maximum values of 90.7% and 85.1%, respectively, at 1.9 V, suggesting the ideal match between the two reactions. In addition, compared to CO₂RR-OER, the facilitated overall kinetics of CO₂RR-HMFOR also sharply reduces the reaction time by 60% (Figure S18, Supporting Information). Of note, the output value is significantly increased from 4.82 to 6.02 dollars per kWh after substituting OER with HMFOR (Figure S19 and Table S2, Supporting Information). We also tested the durability of the CO₂RR-HMFOR co-electrolysis system. During seven consecutive cycles with near-unity conversion of HMF, the FEs of HCOOH and FDCA were well maintained above 80% and 85%, respectively, demonstrating its desired stability (Figure 5c).

As a step further, a commercial Si solar panel was employed to drive the CO₂RR-HMFOR system under simulated sunlight (Figures S20 and S21, Supporting Information). A multimeter was used to measure the potential drop at the anode and cathode of the cell to assess the voltage of solar-driven electrolysis, and the cell voltage was fixed at 1.9 V. As depicted in Figure 5d, high FEs of HCOOH (≈80%) and FDCA (≈85%) fluctuate in a narrow range during the cyclic test, similar to the result of direct electrolysis. Moreover, the production amounts of FDCA and HCOOH increased linearly after each cycle, and finally reached 726.8 and 2715.1 μmol, respectively. We also measured the solar-to-FDCA conversion efficiency (η_{FDCA}) and solar-to-HCOOH conversion efficiency (η_{HCOOH}). By virtue of the efficient electrodes and coupling electrolysis strategy, high η_{FDCA} up to 1.4% was achieved with 0.8% η_{HCOOH} , strongly convincing the viability of the solar-driven CO₂RR-HMFOR system.

3. Conclusion

In summary, we proposed an efficient coupling strategy that substitutes the sluggish OER with selective oxidation of HMF to FDCA in the overall CO $_2$ electrolysis. Impressively, high Faradaic efficiencies up to 96.7% and 94.7% were achieved in the anodic HMFOR and cathodic CO $_2$ RR, respectively. As revealed by the in-situ EIS and Raman spectroscopic measurements, the Ni sites in the NiCo $_2$ O $_4$ @NF anode go through a cyclic transformation of Ni $^{2+}\leftrightarrow$ Ni $^{3+}$ with enhanced adsorption of OH $^-$, which accelerates

the oxidation of HMF. In the CO_2RR -HMFOR co-electrolysis system, the energy requirement was significantly reduced by 22.9% compared to that for CO_2RR -OER. Moreover, with the solar-driven electrolyser, the CO_2RR -HMFOR couple exhibited high solar energy conversion efficiency of 1.4% and 0.8% for FDCA and HCOOH, respectively, with satisfying durability. This work highlights the feasibility of coupling strategy in enhancing the energy efficiency of CO_2 electrolysis. We hope that this enlightening investigation can propel CO_2 electrolysis technique toward industrial application.

Acknowledgements

This work was financially supported by Petrochina Lanzhou Petrochemical Company (Project number: LZSYHG-2023-JS-54), the National Natural Science Foundation of China (grant no. 21790052), and the 111 Project of China (D17003).

Conflicts of Interest

The authors declare no conflict of interest.

Author Contributions

Fangyun Su: data curation (equal), formal analysis (lead), investigation (equal), resources (lead), validation (equal). Zixian Ye: data curation (equal), formal analysis (equal), investigation (equal), writing—original draft (supporting). Zhenhai Zhao: data curation (equal), validation (equal). Hongyu Jiao: formal analysis (supporting), funding acquisition (supporting), investigation (supporting). Kefeng Wu: data curation (equal), investigation (supporting), methodology (supporting), validation (supporting). Jiawang Di: data curation (supporting), validation (equal), Yu Li: conceptualization (lead), formal analysis (lead), funding acquisition (equal), methodology (lead), supervision (lead), writing—original draft (lead), writing—review and editing (lead). Tongbu Lu: conceptualization (equal), funding acquisition (lead), supervision (equal).

Data Availability Statement

The data that support the findings of this study are available from the corresponding author upon reasonable request.

Keywords: biomass oxidation · carbon dioxide reduction · coupling strategy · electrocatalysis

- L. Dong, X. Hu, Y. Du, R. Ge, G.-P. Hao, A. H. Lu, J. Mater. Chem. A 2021, 9, 17821.
- [2] S. Jung, Y.-K. Park, E. E. Kwon, J. CO2 Util. 2019, 32, 128.
- [3] M. Li, C. Yan, R. Ramachandran, Y. Lan, H. Dai, H. Shan, X. Meng, D. Cui, F. Wang, Z.-X. Xu, Chem. Eng. J. 2022, 430, 133050.
- [4] T. Tran-Phu, R. Daiyan, Z. Fusco, Z. Ma, R. Amal, A. Tricoli, Adv. Funct. Mater. 2020, 30, 1906478.
- [5] B. Zhang, S. Chen, B. Wulan, J. Zhang, Chem. Eng. J. 2021, 421, 130003.



- [6] G. Wang, J. Chen, Y. Ding, P. Cai, L. Yi, Y. Li, C. Tu, Y. Hou, Z. Wen, L. Dai, Chem. Soc. Rev. 2021, 50, 4993.
- [7] K. Zhao, X. Quan, ACS Catal. 2021, 11, 2076.
- [8] X. Wei, Y. Li, L. Chen, J. Shi, Angew. Chem., Int. Ed. 2021, 60, 3148.
- [9] Y. Li, C.-Z. Huo, H.-J. Wang, Z.-X. Ye, P.-P. Luo, X.-X. Cao, T.-B. Lu, Nano Energy 2022, 98, 107277.
- [10] J. Na, B. Seo, J. Kim, C. W. Lee, H. Lee, Y. J. Hwang, B. K. Min, D. K. Lee, H.-S. Oh, U. Lee, Nat. Commun. 2019, 10, 5193.
- [11] S. Verma, S. Lu, P. J. A. Kenis, Nat. Energy 2019, 4, 466.
- [12] Y. Li, T.-B. Lu, Mater. Chem. Front. 2024, 8, 341.
- [13] X. Li, W. Kang, X. Fan, X. Tan, J. Masa, A. Robertson, Y. Jung, B. Han, J. Texter, Y. Cheng, B. Dai, Z. Sun, Innovation 2025, 3, 100807.
- [14] P. Gallezot, Chem. Soc. Rev. 2012, 41, 1538.
- [15] D. R. Dodds, R. A. Gross, Science 2007, 318, 1250.
- [16] B. You, X. Liu, N. Jiang, Y. Sun, J. Am. Chem. Soc. 2016, 138, 13639.
- [17] Y. Yang, T. Mu, Green Chem. 2021, 23, 4228.
- [18] D. A. Giannakoudakis, J. C. Colmenares, D. Tsiplakides, K. S. Triantafyllidis, ACS Sustainable Chem. Eng. 2021, 9, 1970.
- [19] T. Wei, W. Liu, S. Zhang, Q. Liu, J. Luo, X. Liu, Chem. Commun. 2023, 59,
- [20] H. Zhang, G. Qi, W. Liu, S. Zhang, Q. Liu, J. Luo, X. Liu, Inorg. Chem. Front. 2023. 10. 2423.
- [21] M. Yang, G. Meng, H. Li, T. Wei, Q. Liu, J. He, L. Feng, X. Liu, J. Colloid Interface Sci. 2023, 652, 155.
- [22] X. Huang, J. Song, M. Hua, Z. Xie, S. Liu, T. Wu, G. Yang, B. Han, Green Chem. 2020, 22, 843,
- [23] Y. Xie, Z. Zhou, N. Yang, G. Zhao, Adv. Funct. Mater. 2021, 31, 2102886.
- [24] K. Gu, D. Wang, C. Xie, T. Wang, G. Huang, Y. Liu, Y. Zou, L. Tao, S. Wang, Angew. Chem., Int. Ed. 2021, 60, 20253.
- [25] Z. Zhang, K. Deng, ACS Catal. 2015, 5, 6529.
- [26] A. J. J. E. Eerhart, A. P. C. Faaij, M. K. Patel, Energy Environ. Sci. 2012, 5, 6407.
- [27] Y. Xiong, S. Hu, J. Jiang, Y. Liu, W. Zhao, X. Ji, C. Chen, M. Fan, K. Wang, Chem. Eng. J. 2024, 499, 156320.

- [28] R. Ge, Y. Wang, Z. Li, M. Xu, S.-M. Xu, H. Zhou, K. Ji, F. Chen, J. Zhou, H. Duan, Angew. Chem., Int. Ed. 2022, 61, e202200211.
- [29] J. Bi, Q. Zhu, W. Guo, P. Li, S. Jia, J. Liu, J. Ma, J. Zhang, Z. Liu, B. Han, ACS Sustainable Chem. Eng. 2022, 10, 8043.
- [30] D. Yang, Q. Zhu, B. Han, Innovation 2020, 1, 100016.
- [31] S. Verma, B. Kim, H.-R. M. Jhong, S. Ma, P. J. A. Kenis, ChemSusChem 2016, 9, 1972.
- [32] C. Chen, J. F. Khosrowabadi Kotyk, S. W. Sheehan, Chem 2018, 4, 2571.
- [33] M. J. Kang, H. Park, J. Jegal, S. Y. Hwang, Y. S. Kang, H. G. Cha, Appl. Catal. B: Environ. 2019, 242, 85.
- [34] Y. Feng, H. Guo, R. L. Smith, X. Qi, J. Colloid Interface Sci. 2023, 632, 87.
- [35] Q. Hu, X. Huang, Z. Wang, G. Li, Z. Han, H. Yang, P. Liao, X. Ren, Q. Zhang, J. Liu, C. He, Small 2020, 16, 2002210.
- [36] X. Zou, J. Chen, Z. Rui, H. Ji, Appl. Catal. B: Environ. 2020, 273, 119071.
- [37] B.-C. He, C. Zhang, P.-P. Luo, Y. Li, T.-B. Lu, Green Chem. 2020, 22, 7552.
- [38] Y. Lu, T. Liu, Y.-C. Huang, L. Zhou, Y. Li, W. Chen, L. Yang, B. Zhou, Y. Wu, Z. Kong, Z. Huang, Y. Li, C.-L. Dong, S. Wang, Y. Zou, ACS Catal. 2022, 12, 4242.
- [39] F. Hu, S. Zhu, S. Chen, Y. Li, L. Ma, T. Wu, Y. Zhang, C. Wang, C. Liu, X. Yang, L. Song, X. Yang, Y. Xiong, Adv. Mater. 2017, 29, 1606570.
- [40] C. Huo, X. Cao, Z. Ye, Y. Li, T. Lu, ChemCatChem 2021, 13, 4931.
- [41] Y. Song, W. Xie, Y. Song, H. Li, S. Li, S. Jiang, J. Y. Lee, M. Shao, Appl. Catal. B: Environ. 2022, 312, 121400.
- [42] Y. Lu, C.-L. Dong, Y.-C. Huang, Y. Zou, Z. Liu, Y. Liu, Y. Li, N. He, J. Shi, S. Wang, Angew. Chem. Int. Ed. 2020, 59, 19215.
- [43] Y. Lu, C.-L. Dong, Y.-C. Huang, Y. Zou, Y. Liu, Y. Li, N. Zhang, W. Chen, L. Zhou, H. Lin, S. Wang, Sci. China Chem. 2020, 63, 980.

Manuscript received: March 14, 2025 Revised manuscript received: April 24, 2025 Version of record online: June 26, 2025